

Coupled Microelectromechanical Drum Resonators for Reservoir Computing via Sideband Pumped Phonon-Cavity Dynamics

Theresa Farah¹, Loïc Flis¹, Pierre Laly¹, Guo-En Chang², Jun-Yu Ou³, Yoshishige Tsuchiya³, Yan Pennec¹, Bahram Djafari-Rouhani¹, and Xin Zhou^{1,*}

¹CNRS, University of Lille, Centrale Lille, Univ. Polytechnique Hauts-de-France, UMR 8520 IEMN, F-59000 Lille, France

²Department of Microelectronics, National Yang Ming Chiao Tung University, Hsinchu City 300093, Taiwan.

³University of Southampton, Southampton SO17 1BJ, United Kingdom

*xin.zhou@cnrs.fr

ABSTRACT

Reservoir computing is a bio-inspired machine learning paradigm that exploits the intrinsic dynamics of nonlinear systems with fading memory for efficient temporal information processing. Microelectromechanical resonators offer a promising platform for reservoir computing as they inherently possess the requisite nonlinear and temporal properties while also facilitating the integration of sensing and computing within a single platform. In this work, we experimentally demonstrate a physical reservoir computing platform based on two capacitively coupled drum resonators, operating in the MHz frequency regime. Taking advantage of the concept of phonon-cavity electromechanics, a pump tone is applied at the sideband of the phonon cavity while probing one of the coupled modes, analogous to optomechanical systems, thereby creating nonlinear dynamics in energy transfer between the two resonators. Physical reservoir computing is implemented by exploiting the nonlinear response induced through pump amplitude modulation in combination with a time-delay feedback loop, and the performance is evaluated using both parity and Normalized Auto-Regressive Moving Average benchmarks. This work demonstrates a compact microelectromechanical platform for the integration of sensing and reservoir computing. Moreover, the sideband pumping scheme can further extend conventional single resonator reservoir computing to a multimode architecture.

1 Introduction

Reservoir Computing is a bio-inspired machine learning paradigm designed for processing complex time-series data¹⁻³. It has been successfully applied to a diverse range of temporal tasks, including chaotic time-series prediction, speech recognition, and signal classification. As a simplified framework derived from Recurrent Neural Networks (RNNs)^{4,5}, reservoir computing fixes the internal weights of the reservoir and only requires the output layer weights to be trained by using simple linear regression. It therefore significantly reduces computational costs while circumventing the vanishing gradient problems typical of traditional RNN training. A physical system used to implement a reservoir must exhibit two key properties: nonlinearity and fading memory^{6,7}. Nonlinearity is required to project input signals into a high-dimensional state space, enabling complex data to become linearly separable at the readout layer. Fading memory is essential for processing temporal sequences, as it establishes a connection between the current reservoir state and recent past inputs. To date, reservoir computing has been demonstrated across a wide range of hardware platforms, including photonic and optoelectronic systems⁸⁻¹⁰, robotics^{11,12}, memristor arrays¹³, spintronic¹⁴⁻¹⁶. More recently, reservoir computing has been further extended beyond classical systems to quantum platforms, including quantum oscillators and nonlinear oscillators coupled to quantum systems^{17,18}.

Micro-Electro-Mechanical Systems (MEMS), which enable mechanical degrees of freedom to be coupled with electrical signals, constitute a promising platform for reservoir computing¹⁹⁻²³. MEMS naturally possess the two essential properties required for reservoir computing: intrinsic nonlinearity arising from geometric and material constraints (such as the Duffing nonlinearity) effects, and fading memory facilitated by the finite decay time of their mechanical resonances²⁴⁻²⁶. In addition, MEMS devices can be designed as scalable architectures and are easily integrated with modern CMOS (Complementary Metal–Oxide–Semiconductor) platforms²⁷. Beyond these advantages, one of the most compelling motivations for developing MEMS-based reservoir computing is its potential to combine sensing and computing within a single platform^{28,29}. Such integration will overcome the inefficiencies of conventional architectures, where the physical separation of sensing and process-

ing units leads to additional energy consumption and latency due to intensive data transfer. To date, MEMS-based physical reservoir computing has been experimentally implemented primarily using single electromechanical resonators, exploiting driving-force modulation in the Duffing nonlinear regime¹⁹ and stiffness modulation techniques²¹. Only a limited number of studies have explored reservoir computing in coupled MEMS systems. These efforts include numerical investigations of reservoir performance in coupled resonators³⁰ and experimental studies evaluating memory capacity in coupled triple-resonator configurations²³. However, they rely on mechanical coupling and require the resonators to have closely matched resonance frequencies, which places stringent demands on nanofabrication and poses challenges for scaling to higher integration densities.

In this work, we experimentally demonstrate a novel reservoir computing scheme based on coupled microelectromechanical resonators by exploiting concepts from phonon-cavity electromechanics^{31,32}. The device employed is a double-drum electromechanical system consisting of two capacitively coupled membrane resonators operating in the MHz frequency regime^{33,34}. Drawing an analogy to two-tone operation in optomechanical systems³⁵, we apply a pump tone at the sideband of the phonon-cavity while probing one of the coupled modes, thereby inducing nonlinear dynamics in the phonon transfer between the two vibrational modes³⁴. By modulating the pump amplitude and implementing a time-delay feedback loop, we demonstrate reservoir computing by probing one of the coupled drum resonators and evaluating both parity and NARMA benchmarks. The unique device design and pump amplitude modulation scheme point toward a compact MEMS platform for co-integrated sensing and reservoir computing. Moreover, the proposed scheme does not require the resonance frequencies to fall within a narrowly distributed range and is not limited to the specific double-drum design. It can be easily extended to other mechanically coupled resonator arrays and multimode optomechanical systems, in both the classical and quantum regimes.

2 Results

2.1 Double-drum resonator and setup for reservoir computing

The microelectromechanical system used to perform reservoir computing in this work is a double-drum resonator, consisting of two suspended membrane electromechanical resonators, as shown in Fig. 1(a)–(c). A suspended aluminum (Al) membrane serves as a capacitively coupled top gate to the underlying silicon nitride (SiN) drum microelectromechanical resonator^{33,34}. In order to excite mechanical vibrations, electrostatic forces are generated by applying a combination of a DC voltage V_{dc} and an AC voltage V_{ac} . We exploit the microwave optomechanical interferometry to simultaneously readout the vibrations of both drums, as shown in Fig. 1(e). Microwave photons at a frequency $\omega_c = 6$ GHz are shined to the double-drum resonator through a 50 Ohm transmission line. The reflected microwave signal, carrying information of the mechanical vibrations at frequency $\omega_c + \Omega$, is readout by using a lock-in amplifier after frequency down-conversion³³. Mechanical mode vibrations are therefore measured in volts in our experiment. Using this readout scheme, the double-drum resonator is initially characterized in its linear operating regime. The SiN drum has a resonance frequency of $\Omega_{SiN}/(2\pi) \approx 12.265$ MHz and a quality factor of $Q_{SiN} \approx 1.3 \times 10^4$. The Al drum resonates at the frequency $\Omega_{Al}/(2\pi) \approx 6.13$ MHz with a quality factor $Q_{Al} \approx 237$. All measurements are carried out at room temperature and under vacuum conditions, $\approx 6 \times 10^{-6}$ mbar.

The reservoir used for computing is constructed from virtual nodes based on a single double-drum resonator acting as the physical node. The creation of virtual nodes are inspired by the conventional time domain multiplexing method implemented in previous works^{19,36}. A standard time-delay loop is implemented using a field-programmable gate array (FPGA), which adds a time delay τ to the detected mechanical vibration $x(t)$ from the output of the nonlinear element and feeds it back to the input of the resonator in the form of driving forces. The virtual nodes are created by mapping a predefined mask $m(t)$ onto the input data $u(t)$. The masked input is then multiplexed with the delayed output of the physical element, $x(t - \tau)$, and combined through a multiplier to generate additional modulations on the driving forces, acting on the double-drum resonator.

2.2 Nonlinear behavior generated by sideband pumping in phonon-cavity electromechanics

The key concept of phonon-cavity electromechanics is to manipulate coherent energy transfer between two coupled mechanical vibration modes, Ω_1 and Ω_2 , by selecting the mode having the higher resonance frequency ($\Omega_1 > \Omega_2$) and pumping it at its sideband $\Omega_1 \pm \Omega_2$ ^{31,32,34,37}. It inherits rich physics from optomechanics, enabling cooling of mechanical vibration modes, amplification of phonon occupancy, and the creation of controllable interference effects³⁸. In this double-drum resonator, we choose the SiN drum as the phonon-cavity mode and pump it at its blue sideband, at the frequency $\Omega_p = \Omega_1 + \Omega_2 + \Delta = \Omega_{Al} + \Omega_{SiN} + \Delta$. Here the Δ is defined as small frequency detuning. Additional to the pump tone, a second tone with small amplitudes is introduced to probe one of the mode with a small frequency detuning δ from the resonance, either $\Omega_d \approx \Omega_1 + \delta$ or $\Omega_d \approx \Omega_2 + \delta$, placing the double-drum under a two-tone driving scheme, as shown in Fig. 2 (a) and (b). Because of frequency mixing effects, the probe and pump tones generate vibration phonons in the unprobed mode, as indicated by the process $\langle 1 \rangle$. These phonons are subsequently projected back onto the probed mode by the pump, where they interfere with the probe tone.

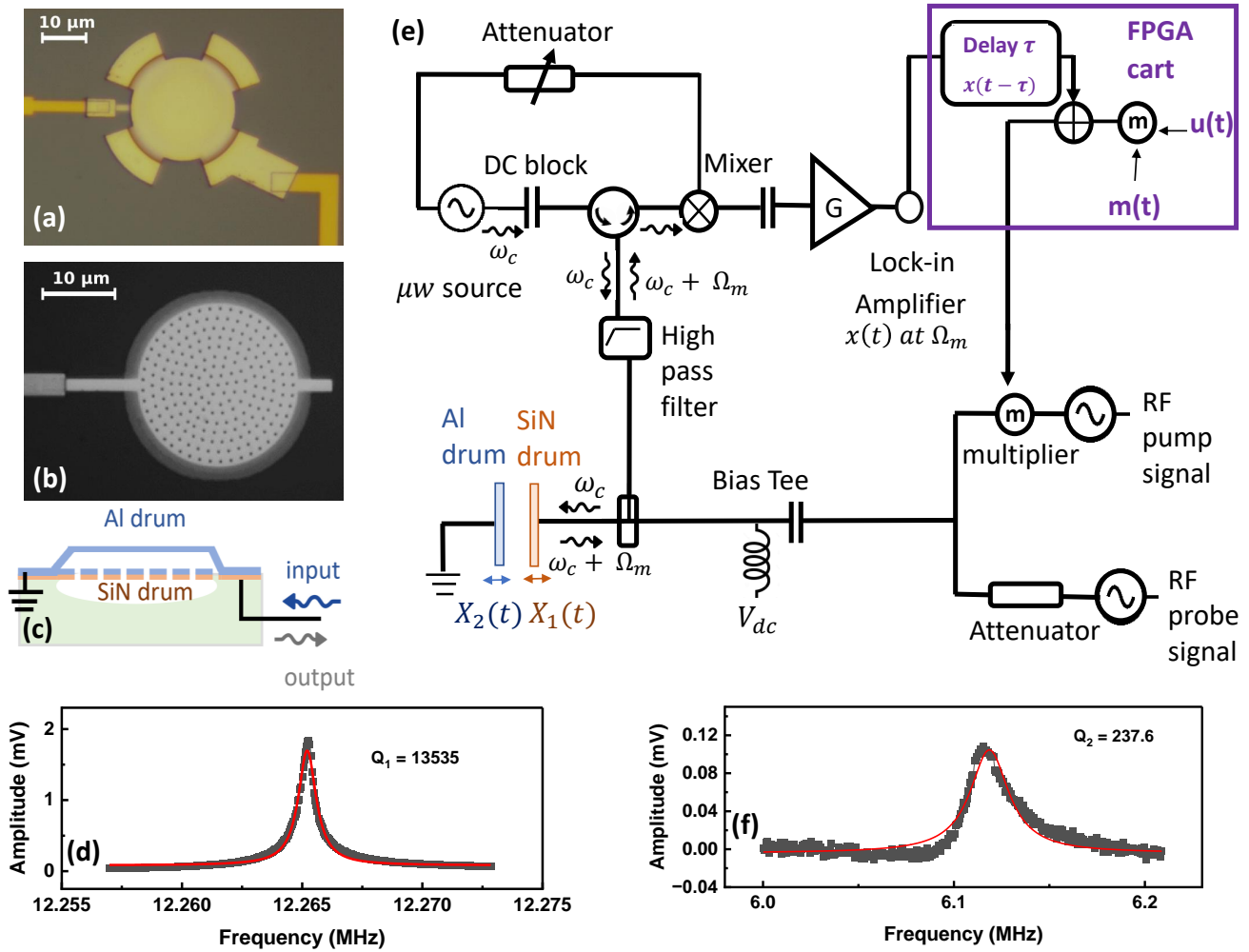


Figure 1. Experiment setup. (a) Optical image of the Al drum resonator which is suspended over the SiN circular drum by the means of 4 support feet. (b) Optical image of the bottom SiN membrane resonator, covered with an Al thin film. There is no physical connection between the two drums. (c) Cross sectional view of the electromechanical system. (d) and (f) The mechanical responses of the SiN and Al drum resonators are measured under a DC bias of $V_{dc} = 4$ V, with AC drive of $V_d = 6$ mV and 80 mV, respectively, each attenuated by 20 dB. (e) Schematic diagram of the measurement setup. The mechanical displacement is read out using a lock-in amplifier via microwave optomechanical interferometry. The output of the FPGA is used to modulate the pump signal through a multiplier.

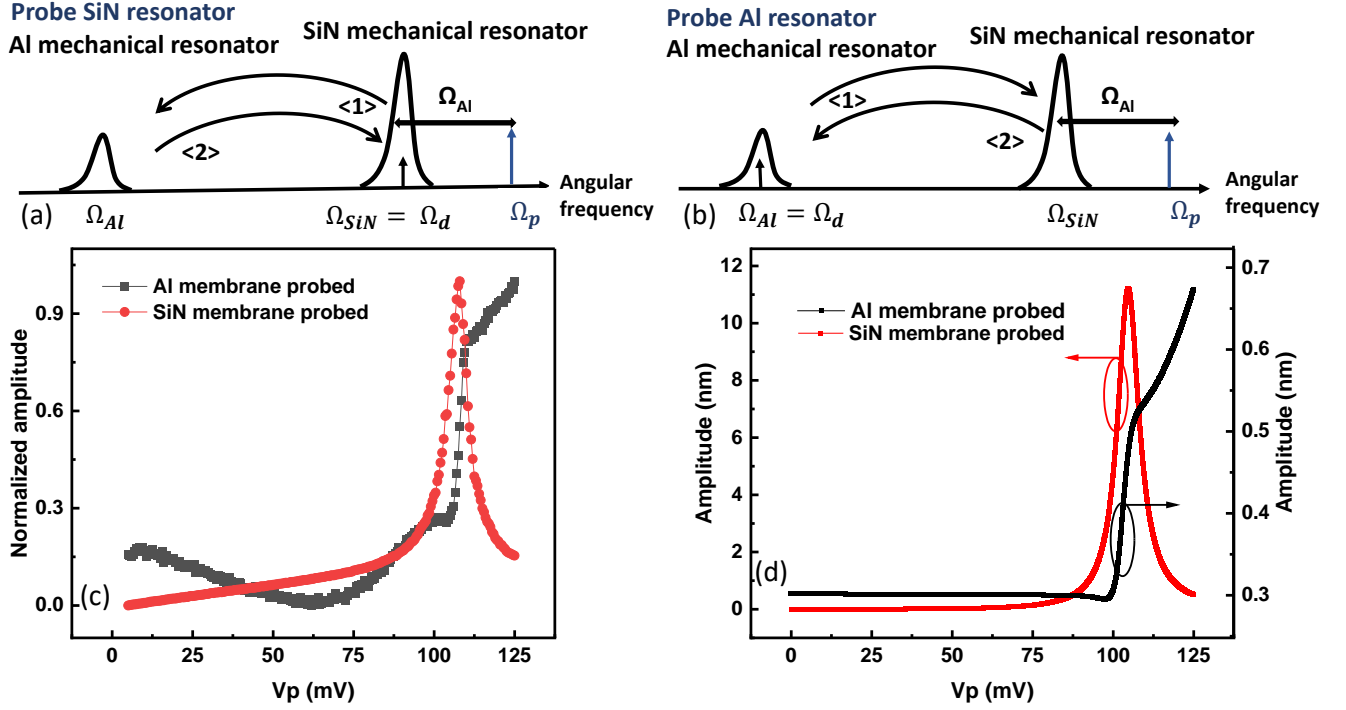


Figure 2. Diagram of the blue sideband pumping scheme while probing (a) the phonon-cavity SiN drum and (b) the Al membrane resonator, respectively. (c) The measured normalized response mechanical responses as a function of the pump amplitude. The background contribution has been subtracted using the measured minimum amplitude as a reference. The black (red) curve is measured by probing Al (SiN) drum at $\Omega_d/(2\pi) = 6.12$ MHz ($= 12.25$ MHz) with amplitude $V_d = 80$ mV (6 mV) attenuated by 20 dB, with $\Omega_p/(2\pi) = 18.38$ MHz and $V_{dc} = 4$ V. (d) Analytical calculation results of the mechanical amplitude as a function of the pump amplitude in both probing cases, by using experimental parameters.

The two-tone dynamics of the double-drum resonator are described by the following coupled equations of motion:

$$\begin{aligned} \ddot{X}_1 + \gamma_1 \dot{X}_1 + \Omega_1^2 X_1 &= \frac{V_{ac} V_{dc}}{m_1 d} C_{go} \left[1 - 2 \frac{(X_2 - X_1)}{d} \right], \\ \ddot{X}_2 + \gamma_2 \dot{X}_2 + \Omega_2^2 X_2 &= \frac{V_{ac} V_{dc}}{m_2 d} C_{go} \left[-1 + 2 \frac{(X_2 - X_1)}{d} \right], \end{aligned} \quad (1)$$

where index 1 and 2 refer to each of the SiN and Al membrane respectively. The $m_{1,2}$ denotes the effective mass of the resonator, d the distance between two drums, $X_{1,2}$ the mechanical displacement, C_{go} coupling capacitance between two drums at $X_{1,2}=0$, and γ the damping rate. Within the capacitive coupling scheme, the electrostatic force acting on the resonator arises from the term $V_{dc} V_{ac} \partial C_g(x_{1,2}) / \partial x_{1,2}$ ³³. In the two-tone driving scheme, V_{ac} is given by $V_p \cos(\Omega_p t) + V_d \cos(\Omega_d t)$. In the case of probing the SiN drum resonator, $\Omega_d = \Omega_1 + \delta = \Omega_{SiN} + \delta$, the displacement of the probed resonator can be obtained by solving the Eq. 1. To do so, we re-write variables in complex form, such as $X_1(t) = \frac{x_1(t)}{2} e^{-i\Omega_d t} + c.c.$, and x_1 arrives

$$\begin{aligned} x_1 &= \frac{f_d}{2m_1 \Omega_1} \frac{1}{\chi_1 + \frac{|f_p|^2 \chi_2}{4m_1 m_2 d^2 \Omega_1 \Omega_2}}, \\ x_2 &= \frac{f_p^*}{2m_2 \Omega_2} \frac{x_1}{d} \chi_2, \end{aligned} \quad (2)$$

where $f_d = \frac{C_{g0} V_{dc} \mu_d}{d}$ and $f_p = \frac{C_{g0} V_{dc} \mu_p}{d}$ are the amplitudes of the probe and pump forces respectively, the parameter μ represents the complex amplitude of the pump or probe tone, and the $c.c.$ denotes the complex conjugate term. The $\chi_1 = \frac{1}{-\delta - i\frac{\gamma_1}{2}}$ and

$\chi_2 = \frac{1}{\delta - \Delta - i\frac{\gamma_2}{2}}$ are the mechanical susceptibilities of the drum resonators when probing the SiN phonon-cavity. The entire derivation process has been reported in our previous work³⁴. The calculation results corresponding to the case of probing the Al drum are provided in the Supporting Information (SI). From the displacement expressions of both drums, x_1 and x_2 , as given in Eq.2, the blue sideband pump brings nonlinear amplifications of the phonons for the probed mode through creating frequency dependent constructive interference. Such interference arises from pump induced coherent phonon cycling between the two coupled modes, and the effective constructive interferences windows depend on the frequency detunings δ and Δ relative to the mechanical damping rates γ_1 and γ_2 . The pump tone functions as a phonon bus, transferring the energy from one mode to the other, in the coupled resonators.

To take advantage of this pump induced nonlinear behavior for reservoir computing, we exploit the fact that the sideband pump amplitude has a effect on shifting Ω_{SiN} , so called optical spring effect in optomechanics^{34,38}. More details can be found in SI part. This effect arises from the fact that the sideband pump amplitude modifies the effective susceptibility of the coupled mechanical resonators. It is worth emphasizing that this pump induced effect on Ω_{Al} can be neglected in this double-drum system. Because the Al drum has a relatively large bandwidth (damping rate), $\gamma_{Al} \approx 2\pi \times 25.9$ kHz, small variations in the resonance frequency are not easily observed. To do so, we set the pump frequency to $\Omega_p = \Omega_{SiN} + \Omega_{Al}$, where both resonances Ω_{SiN} and Ω_{Al} are obtained by measuring mechanical responses at the sideband pump amplitude $V_{pc} = 105$ mV. We then set the probe tone frequency to either $\Omega_d = \Omega_{SiN}$ or $\Omega_d = \Omega_{Al} +$ a few kHz, and measure its amplitude as a function of V_p . The detected probe signals exhibit clear nonlinear constructive interference induced by variations in the pump amplitude, as shown in Fig.2 (c). When the pump amplitude deviates far from the calibrated value $V_{pc} = 105$ mV, the interference between the probe tone and the phonons projected back from the unprobed mode becomes less effective due to shifts in Ω_{SiN} , which induce frequency detunings δ and Δ in Eq.2. Because the two drum resonators have very different damping rates, the pump induced nonlinear behaviors are quite different when probing the cavity mode versus the Al drum. The bandwidth $\gamma_{SiN} \approx 2\pi \times 944$ Hz is much smaller than the resonance-frequency shift induced by variations in the pump amplitude (see SI). Consequently, when the probe tone is initially biased at Ω_{SiN} corresponding to $V_{pc} = 105$ mV, both increases and decreases in the pump amplitude can shift Ω_{SiN} over a frequency rang of 7 kHz, making the probe tone to move out of resonance. However, the probe tone can still be amplified through constructive interference, since this frequency shift lies within γ_{Al} . When probing the Al drum, although the probe tone always remains within the bandwidth, clear constructive interference can be observed only when the resonance shift relative to the value calibrated at V_{pc} lies within γ_{SiN} . We also noticed that the detected amplitudes of Al drum exhibiting small fluctuations for $V_p < 75$ mV. It may be induced by fluctuations in the background noise carried by the pump tone. Fig. 2 (d) presents the calculation results, based on Eq.2, including the pump induced shift of Ω_{SiN} , which are consistent with the experimental observations. These results demonstrate that pump amplitude modulation in the two-tone driving scheme provides a controllable way of inducing nonlinear behavior in the probe tone, in coupled resonators. In the following part, we exploit this nonlinear dynamics for reservoir computing.

2.3 Reservoir computing implementation in the phonon-cavity scheme

In the experiment setting, each input is held for a delay time τ , during which a random binary mask consisting of $N_{mask} = 400$ random values ranging between 0 and 1 is applied with a sampling period of θ , yielding $\tau = N_{mask}\theta$. The delay feedback loop provides the reservoir states with fading memory by coupling the current mechanical response $x(t)$ to its delayed response $x(t - \tau)$, thereby creating a recurrent loop in the virtual neural network. As shown in the Fig.1 (e), both the masked input $u(t)m(t)$ and the delayed mechanical responses $x(t-\tau)$ modulate the pump amplitude by combining the FPGA output with the AC signal through a multiplier. This modulation can be described by expressions of

$$V_p(t) \propto V_{p0}[\alpha_1 u(t)m(t) + \alpha_2 [x(t - \tau) - x_0] + offset]. \quad (3)$$

The values of the constants α_1 , α_2 and *offset* are fixed by programmed MATLAB codes to avoid the saturation of the FPGA card, x_0 denotes the preset offset in the measurement. These values define the modulation range of the pump amplitude that can generate the nonlinearity required for implementing reservoir computing.

2.4 The Parity Benchmark

The performance of the system was first evaluated using the parity benchmark, which tests the short-term memory capacity of the reservoir and its ability to perform nonlinear mixing of past input states. This benchmark consists of a sequence of random binary input values $u(t)$, taking either +1 or -1, each held for a duration τ . The target n^{th} order parity benchmark output is computed as follows :

$$P_n(t) = \prod_{i=0}^{n-1} u[t - (i + \delta)\tau]. \quad (4)$$

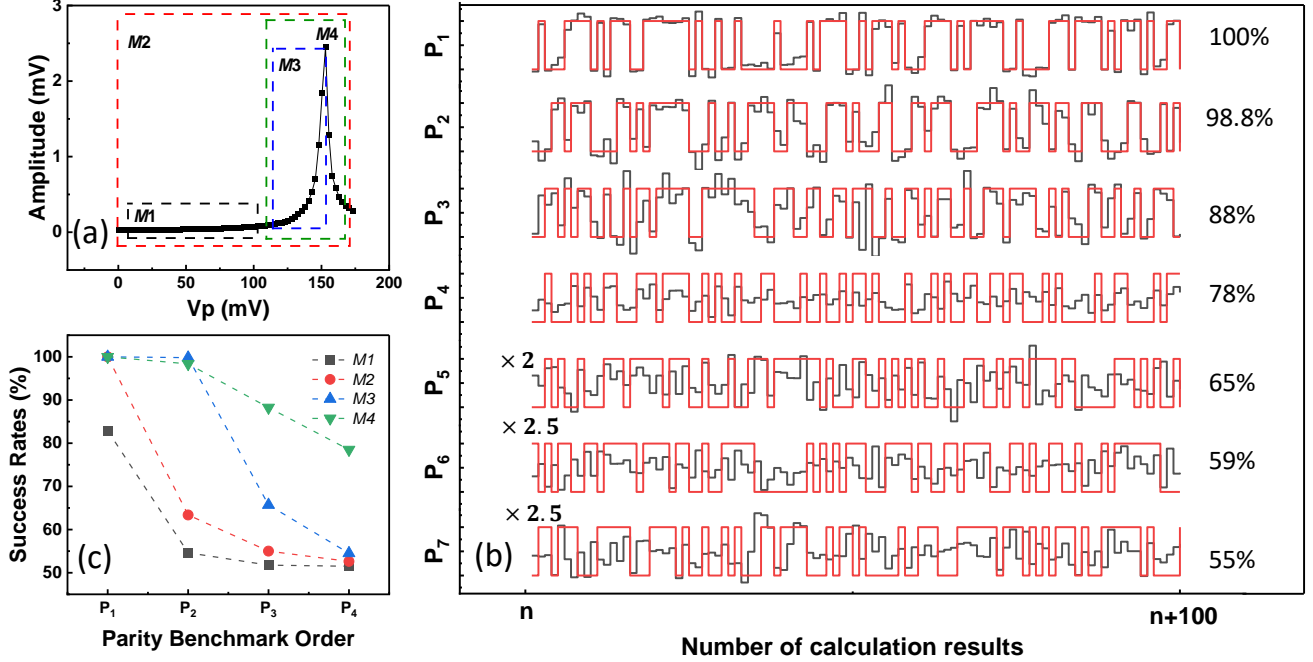


Figure 3. Reservoir Computing based on the sideband pumping mechanism while probing the SiN drum with $\Omega_d/(2\pi) = 12.26$ MHz, $V_d = 6$ mV, $\Omega_p/(2\pi) = 18.38$ MHz and $V_{dc} = 4$ V. (a) The detected mechanical displacement of the probed SiN membrane as a function of the amplitude of the blue pump signal. The curve is divided into 4 modulation windows $M1$, $M2$, $M3$, and $M4$ showcasing different profile variations depending on the interval of the blue pump voltage. (b) Comparison between the predicted output by our reservoir computing scheme (black lines) and the target ideal output of the parity benchmark (red lines) for the first 7 orders of the parity benchmark in the case of the modulation window $M4$. (c) Success rates obtained for the first 4 orders of the Parity Benchmark corresponding to each of the 4 modulation windows.

In the experiment, we set $\delta = 0$. The objective is to train the output weights of the system to provide an output which can be as close as possible to the target output P_n . For $n > 1$, the parity function is nonlinear separable and the task requires the reservoir to store information about a nonlinear transform of previous inputs¹⁹.

Probing the SiN phonon-cavity We first implement the nonlinear amplification scheme by probing the phonon cavity with a weak probe tone while simultaneously applying a blue-sideband pump, as shown in Fig.3 (a). Based on this measurement results and Eq.3, we select the modulation range of the applied pump force by adjusting the setup parameters α_1 , α_2 , *offset* and V_{p0} . This enables us to perform separate reservoir-computing measurements under different nonlinear operating regimes. The $M1$ is the window characterized by a relatively linear variation of the response as a function of the pumping force, $M2$ is the whole curve with all the linear and nonlinear profiles, $M3$ is where the nonlinear amplification occurs due to the constructive interferences. The $M4$ corresponds to a combination of the amplified response and a subsequent drop induced by the Ω_{SiN} shifting out of the effective interference window.

Fig.3 (b) shows one example of the comparison between the target values $P_n(t)$ and the predicted values by the neural network, which are obtained in the modulation window $M4$, with $\theta = 100 \mu s$ and a period of $\tau = N_{mask}\theta = 40$ ms. The values of the constants α_1 , α_2 and *offset* that modulate the electrostatic pump force were set respectively to 0.55, 0.34 and 0.69. The success rates show near-perfect results for the first-order P_1 to the third-order P_3 of the parity benchmark, then the curve becomes more noisy for the P_7 . This decrease of the success rate is linked to the requirement of a higher memory capacity from our device.

Figure 3 (c) presents the reservoir computing results for the different modulation windows described above. The best results are obtained for $M4$ where the characterization curve is strongly nonlinear and where the influence of the interferences are the most dominant. Consequently, the $M3$ modulation window yields the second-best performance due to its nonlinear response profile. However, as for the $M1$ window, very poor results are achieved reaching approximately 50 % starting from P_2 . This is due to the absence of nonlinearity in this modulation window and low signal to noise ratio. Lastly, the window $M2$ in which the

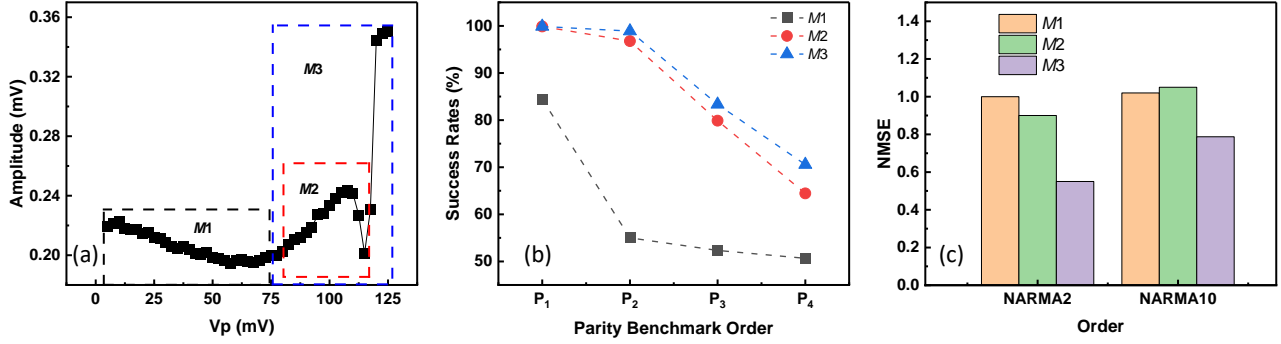


Figure 4. reservoir computing based on the sideband pumping mechanism while probing the Al drum with $\Omega_d/(2\pi) = 6.12$ MHz, $V_d = 80$ mV, $\Omega_p/(2\pi) = 18.38$ MHz and $V_{dc} = 4$ V. (a) The detected mechanical displacements of the probed Al membrane as a function of the variation of the amplitude of the blue pump signal. The curve is divided into three modulation windows of the pump amplitudes the $M1$, $M2$ and $M3$ where the detected probe tone exhibits different variations. (b) Success rates for the first four orders of the parity benchmark (from P_1 to P_4) for the three different modulation windows. (c) The values of the obtained NMSE in the case of NARMA2 and NARMA10 corresponding to each modulation window

force is modulated between 0.5 mV and 175 mV shows also poor results reaching around 60 % at the second-order. In this modulation range, the linear plateau spans a much wider interval than the nonlinear region, reducing the likelihood that the modulated pump amplitude enters the V_p range that generates nonlinear behavior. Consequently, the success rates decrease rapidly, indicating poor reservoir computing performance for this modulation window.

Probing the Al drum resonator We use the same probing method described above for the phonon cavity to obtain the nonlinear amplification curve of the probe tone around the Ω_{Al} , as shown in Fig. 4 (a). This curve was subdivided into 3 different modulation windows: $M1$ marked by a linear plateau fluctuating around a minimum value of 0.2 mV, $M2$ where the curve exhibits a nonlinear amplification up to a maximum of 0.24 mV accompanied by a fast drop and $M3$ that combines the $M2$ window with the sudden jump to a displacement value of 0.34 mV. The reservoir computing studies with these 3 modulation windows were conducted with values of the force modulation parameters α_1 , α_2 and offset respectively 0.56, 0.33 and 0.71. Promising success rates were obtained in the cases of the windows $M2$ and $M3$ due to the nonlinear variation of the characterization curve in each window. Near perfect results were obtained for both P_1 and P_2 in both cases and then it decreases slowly to reach around 70% for the P_4 . As for $M1$, the success rates deteriorated quickly reaching an unsatisfactory 50% starting from the second-order P_2 of the parity benchmark due to the absence of nonlinear variations within this modulation range of the pump force.

2.5 The NARMA Benchmark

The Normalized Auto-Regressive Moving Average (NARMA) benchmark is widely used to evaluate nonlinear processing and fading memory in reservoir computing systems. The key feature of the NARMA benchmark is that the current output is generated through a nonlinear combination of many past inputs and outputs. As a result, it requires the reservoir that combines nonlinear processing with long fading memory³⁹. A generalized version of its input-output relationship for this benchmark is given by:

$$\hat{y}_n(t+1) = 0.3\hat{y}_n(t) + 0.05\hat{y}_n(t) \sum_{i=0}^{n-1} \hat{y}_n(t-i) + 1.5u(t)u(t-n+1) + 0.1 \quad (5)$$

where n is a time-lag parameter. The input $u(t)$ of the system consists of scalar random numbers, drawn from a uniform distribution over the interval $[0, 0.5]$. The \hat{y}_n is the output target. In order to evaluate the performance of the system based on the NARMA benchmark, we compute the Normalised Mean Squared Error (NMSE). Assuming that the target output vector is \hat{y} and the predicted output vector by our reservoir computing is y , we adopt the following definition of the NMSE^{21,40}:

$$MSE(\hat{y}, y) = \frac{1}{N_{lst}} \sum_{t=1}^{N_{lst}} (\hat{y}_t - y_t)^2, \quad (6)$$

$$NMSE(\hat{y}, y) = \frac{MSE(\hat{y}, y)}{MSE(\hat{y}, \text{mean}(\hat{y}))}.$$

	Duffing nonlinearity	Blue sideband pump probe phonon cavity	Blue sideband pump probe Al resonator
θ (μ s)	50	100	100
N_{tr}	1500	1500	1500
N_{lst}	400	400	400
α_1	0.51	0.52	0.36
α_2	0.85	0.35	0.51
offset	0.15	0.67	0.51

Table 1. Reservoir Computing parameters used for NARMA tests, corresponding to different nonlinear schemes.

As demonstrated in previous studies on the parity benchmark, the initial step in designing a reservoir computing framework is to determine the optimal pump force modulation window. Here, we evaluated the system’s NARMA performance across various modulation windows by probing the Al drum resonator via a sideband pumping scheme, as presented in Fig. 4(a). The resulting measurements for each modulation window are shown in Fig. 4(c). The optimal NMSE values were achieved at modulation window $M3$, coinciding with the nonlinear jump where phonon interference effects become dominant. This observation aligns with our previous results from the parity benchmark tests.

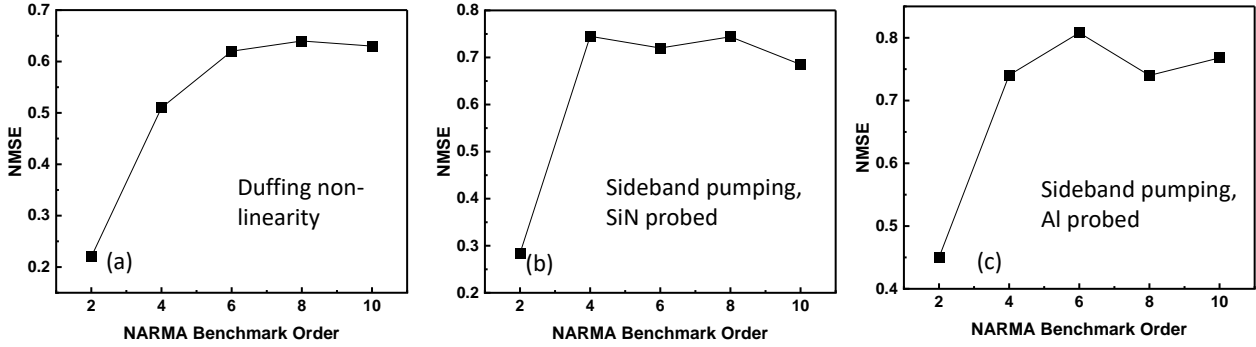


Figure 5. The obtained NMSE values as a function of the order of the NARMA Benchmark in the case of (a) Duffing nonlinearity, and Blue sideband pumping the phonon-cavity while (b) probing the SiN drum (c) probing the Al drum.

By selecting an optimal modulation window that maximizes the system’s nonlinear response, we evaluated various modulation schemes using the NARMA benchmark. The first approach leverages the Duffing nonlinearity, the predominant nonlinear characteristic of microelectromechanical systems, which has been successfully employed for reservoir computing in several prior studies^{19,41}. In our double-drum architecture, we exploit the Duffing properties of a SiN circular resonator. Due to its specific mechanical geometry, this design typically yields a higher nonlinearity coefficient than conventional doubly-clamped beams^{25,42}. The second and third ones are based on the sideband pumping creating nonlinear amplification mechanism while probing respectively the SiN phonon-cavity and Al resonators. The experimental findings are presented in Fig. 5 and details regarding the training and testing parameters can be found in table 1.

In the case of Duffing nonlinearity (Fig. 5(a)), the NMSE increases gradually from 0.2 and converges to approximately 0.6 at the tenth-order NARMA benchmark. The same trend is observed in the sideband pumping experiment while probing SiN (Fig. 5(b)) and Al drums (Fig. 5(c)). It is noticeable that the NMSE increases slightly while probing the SiN drum as it converges to approximately 0.7 and it reaches 0.8 for the NARMA10 in the case of probing the Al drum.

3 Discussion

This double-drum electromechanical resonator exhibits strong potential for high integration density and low driving energy. Because of its compact design, each vibrating element occupies an area of approximately $24 \mu\text{m} \times 24 \mu\text{m}$. And, the coupled-membrane architecture provides strong capacitive coupling ($C_{g0} \approx 9.61 \text{ fF}$), enabling efficient excitation of mechanical

vibrations using a small AC drive voltage. The effective driving voltages applied on the device are $V_p = 326$ mV and $V_d = 0.6$ mV with a DC bias of $V_{dc} = 4$ V. These values are obtained by taking into account the 20 dB attenuation of the driving signal, the 13 dB attenuation of the pump tone, and the voltage gain of the multiplier ($\times 10$ in amplitude) applied to both the driving and pump tones in the input chain. The maximum power consumption to excite the double-drum device for creating the nonlinear operating regime is therefore estimated to be $E_{el} = \frac{1}{2}C_{g0}V^2 = 12.53$ fJ for one input (without interference) in the reservoir computing process, for the case of probing the SiN phonon cavity. To the best of our knowledge, this work demonstrates the lowest energy consumption per input (without interference) among reservoir computing implementations based on micromechanical resonators.

The processing speed for MEMS-based reservoir computing is primarily limited by the decay time of the mechanical response, given by $T_{SiN,Al} = 2Q_{SiN,Al}/\Omega_{SiN,Al}$. To increase the processing speed, the ideal approach is to operate MEMS resonators at higher resonance frequencies while maintaining a lower quality factor. However, an optimal balance between resonance frequency and quality factor is required: excessively low Q values increase mechanical noise and necessitate higher drive amplitudes, leading to increased energy consumptions. In the present double-drum resonator having resonance frequencies in MHz range, such a balance is required. For instance, the SiN drum operates in the > 10 MHz frequency range with a suitable $Q \sim 10^4$, giving the decay time $T_{SiN} \approx 330$ μ s. For characterizing Duffing nonlinearity based reservoir computing, the best success rates are obtained around $\theta = 50$ μ s, having $\theta \approx \frac{T}{5}$ for SiN drum. Under these conditions, approximately five virtual neurons are generated within one oscillation period, consistent with previous report⁷.

In the coupled mechanical resonators based double-tone scheme, whether probing the phonon cavity or the Al drum, we obtain an optimal virtual node separation $\theta = 100$ μ s for both the parity and NARMA benchmarks. In this regime, the $\theta \gg T_{Al} = 12.5$ μ s while $\theta \lesssim T_{SiN} = 330$ μ s. In the delayed feedback system, it is generally expected that when the θ much larger than the decay time T of the nonlinear node, temporal coupling between virtual nodes is lost, causing each node to behave as an effectively self-coupled unit and reducing the diversity of reservoir states. Our experimental results do not contradict this principle. In the present double-drum system, the nonlinear dynamics exploited for reservoir computing processing arise from the energy (in the form of vibration phonons) coherent transfer between two coupled modes. Consequently, although one resonator exhibits a fast decay, the presence of the slower resonator sustains the system in a transient dynamical regime, thereby preserving effective temporal coupling and reservoir state diversity. The coupled resonator design effectively extends the reservoir memory through multimode coupling, even when the virtual node separation exceeds the decay time of the faster resonator.

We compare the performance of this MHz-range double-drum resonator with previously reported reservoir computing implementations using single MEMS resonators operating at kHz frequencies. For the parity benchmark, the success rates achieved in this double-drum resonator with the sideband-pumping approach are slightly lower than those obtained using the Duffing nonlinearity alone. These results are comparable to those reported for MEMS accelerometer based reservoirs³⁹, but remain below the performance achieved with doubly clamped beam MEMS implementations¹⁹. Regarding the NARMA benchmark, our NMSE results do not yet match the good performance of the kHz-range MEMS, particularly those utilizing stiffness modulation techniques^{21,22,41}. We attribute this behavior to additional noise associated with the fast-decaying Al mode, which influences the overall reservoir computing performance of the double-drum system. This work represents the first demonstration of reservoir computing using coupled MEMS resonators operating in the MHz frequency regime. However, the high-frequency operation imposes stricter constraints on the fading memory compared to the kHz systems. Further optimizations of both training algorithm and device design are required to improve performance. One promising direction is to enhance the reservoir computing algorithm at the software level, for example by optimizing post-processing strategies to extend the effective long term memory capacity²¹. In parallel, the mechanical properties of the Al drum could be improved through optimization of the nanofabrication process, such as reducing clamping losses or increasing intrinsic stress to enhance the quality factor and thereby suppress noise and further reducing the required driving forces.

This work presents a novel reservoir computing scheme based on a double-drum resonator system that leverages concepts from phonon-cavity electromechanics. In the two-tone scheme, nonlinear interference effects are induced by applying a pump tone at the blue sideband of the phonon cavity while probing one of the coupled resonators. By exploiting this effect and modulating the pump amplitude, we experimentally demonstrate time delay loop based reservoir computing using two capacitively coupled drum resonators. The pump tone acts as a coherent data bus, generating phonons in the unprobed mode, which are subsequently projected back to the probed mode forming an interference effect. This sideband pumping method allows one of the coupled mode to function as a dedicated sensor, while the detected signals are transduced into mechanical properties, for instance the variations of phonon numbers or resonance frequency, and coherently transferred to the second

drum for reservoir computing. This separation of sensing and processing within a single electromechanical platform advances the development of compact MEMS systems that integrate sensing and computing functionalities. In addition, we would like to emphasize that the proposed reservoir computing scheme based on the sideband pumping technique is not limited to our double-drum resonator architecture and does not require the resonance frequencies of the two coupled resonators to be closely matched. It can be straightforwardly extended to other multimode coupling platforms, including mechanically coupled resonator arrays and optomechanical systems.

4 Materials and methods

Device fabrication: The double-drum electromechanical resonator, measured in this work, consists of two suspended membrane. The device fabrication process begins with a high-resistivity silicon substrate ($>10\text{k } \Omega\cdot\text{cm.}$) covered with a stoichiometric SiN thin film (90 nm in thickness), having ~ 1 GPa tensile stress. To release the SiN membranes from the substrate, circularly symmetric holes with a diameter of 350 nm are first patterned in the SiN layer using electron-beam lithography. A reactive ion etching (RIE) process employing SF_6 and Ar gases is then used to remove the exposed SiN through those patterned holes on the resist. This step is followed by selective isotropic etching of the underlying silicon substrate using XeF_2 (Xenon difluoride), which exhibits a high selectivity between silicon and SiN. This two-step etching process releases the SiN membranes while preserving fully clamped boundary conditions at the edges, forming suspended drum resonators. To form capacitive coupling scheme, about 20 nm Al thin film is deposited on the SiN drum as a conductive layer. The suspended top gate of the SiN drum resonator is fabricated using a polymethyl methacrylate (PMMA) resist layer with a thickness of approximately 350 ± 50 nm which serves as a sacrificial support layer. The PMMA is defined through a soft-bake and reflow process^{33,43}. Subsequently, the top-gate pattern is defined in a second layer of methyl methacrylate (MMA) resist deposited on top of the PMMA layer. The fabrication process is completed by depositing an approximately 550 nm thick Al film, followed by a lift-off process. During lift-off, the sacrificial PMMA support layer is also removed, resulting in a suspended top-gate structure. The SiN drum has a diameter $\approx 22 \mu\text{m}$ and the Al drum has a diameter of $\approx 24 \mu\text{m}$. The separation between the two drums is ≈ 350 nm.

Implementation of measuring equipment: The microwave source used for microwave interferometry measurements is an Rohde & Schwarz SMB100B signal generator, which provides ultra-low phase noise. The microwave power shining to the double-drum through transmission line is around -5 dBm. A Yokogawa GS200 source is used to supply the DC bias voltage V_{dc} . The AC drive signals are generated using a Keysight Technologies 33622A arbitrary waveform generator for the pump tone and a Zurich Instruments UHFLI 600 MHz lock-in amplifier for the probe tone. After frequency down-conversion of the microwave signal to the MHz range, the mechanical displacement excited by the probe tone is detected by the lock-in amplifier as a voltage signal. This signal is then fed back to the input of a AMD Spartan-7 FPGA (XC7S100) to create a time delay τ . It is then added with the masked data (mask $m(t)$) onto the input data $u(t)$ for the output of the FPGA. An AD835 analog multiplier is used to multiply the incident pump signal with the FPGA output, in order to modulate the pump force applied to the double-drum resonator.

Training: The displacement vector, created from the force amplitude modulation, will be linearly combined and give the final output $y(t)$ based on the formula

$$y(t) = W^T x(t). \quad (7)$$

The weight vector W will be trained in a supervised training scheme as to provide a prediction $y(t)$ as close as possible to the target $y_{target}(t)$. The training is done to have the minimizing the mean squared error between $y(t)$ and $y_{target}(t)$ by applying a ridge regression as following:

$$W = y_{target} Z^T (ZZ^T + \lambda I)^{-1} \quad (8)$$

The Z is the data displacement matrix consisting of $x(t)$ and λ is the regularization parameter. When the training of the weight vector W ends, we will test the performance of our system for different inputs^{19,44}. All computing processes are based on 2000 input bits. The first 100 inputs are discarded to eliminate offset effects from previous measurements. The subsequent 1500 inputs are used for training, and the remaining 400 inputs are used for prediction.

References

1. Lukosevicius, M. & Jaeger, H. Overview of reservoir recipes. Tech. Rep., Jacobs University Bremen (2007).
2. Jaeger, H. Adaptive nonlinear system identification with echo state networks. *Adv. neural information processing systems* **15** (2002).

3. Maass, W., Natschläger, T. & Markram, H. Real-time computing without stable states: A new framework for neural computation based on perturbations. *Neural computation* **14**, 2531–2560 (2002).
4. Graves, A. *Long short-term memory: Supervised sequence labelling with recurrent neural networks*, vol. 385 (Springer, Berlin, Heidelberg, 2012).
5. Werbos, P. J. Backpropagation through time: what it does and how to do it. *Proc. IEEE* **78**, 1550–1560 (2002).
6. Samarasinghe, S. *Neural networks for applied sciences and engineering: from fundamentals to complex pattern recognition* (Auerbach publications, 2016).
7. Appeltant, L. *et al.* Information processing using a single dynamical node as complex system. *Nat. communications* **2**, 468, DOI: [10.1038/ncomms1476](https://doi.org/10.1038/ncomms1476) (2011).
8. Paquot, Y. *et al.* Optoelectronic reservoir computing. *Sci. Reports* **2**, 287, DOI: [10.1038/srep00287](https://doi.org/10.1038/srep00287) (2012).
9. Larger, L. *et al.* Photonic information processing beyond turing: an optoelectronic implementation of reservoir computing. *Opt. express* **20**, 3241–3249 (2012).
10. Vandoorne, K. *et al.* Experimental demonstration of reservoir computing on a silicon photonics chip. *Nat. communications* **5**, 3541, DOI: [10.1038/ncomms4541](https://doi.org/10.1038/ncomms4541) (2014).
11. Degraeve, J., Caluwaerts, K., Dambre, J. & Wyffels, F. Developing an embodied gait on a compliant quadrupedal robot. In *2015 IEEE/RSJ International Conference on Intelligent Robots and Systems (IROS)*, 4486–4491, DOI: [10.1109/IROS.2015.7354014](https://doi.org/10.1109/IROS.2015.7354014) (2015).
12. Caluwaerts, K., D’Haene, M., Verstraeten, D. & Schrauwen, B. Locomotion without a brain: Physical reservoir computing in tensegrity structures. *Artif. Life* **19**, 35–66 (2013).
13. Du, C. *et al.* Reservoir computing using dynamic memristors for temporal information processing. *Nat. Commun.* **8**, 2204, DOI: [10.1038/s41467-017-02337-y](https://doi.org/10.1038/s41467-017-02337-y) (2017).
14. Torrejon, J. *et al.* Neuromorphic computing with nanoscale spintronic oscillators. *Nature* **547**, 428–431 (2017).
15. Watt, S., Kostylev, M. & Ustinov, A. B. Enhancing computational performance of a spin-wave reservoir computer with input synchronization. *J. Appl. Phys.* **129**, DOI: [10.1063/5.0033292](https://doi.org/10.1063/5.0033292) (2021).
16. Nakane, R., Tanaka, G. & Hirose, A. Reservoir computing with spin waves excited in a garnet film. *IEEE access* **6**, 4462–4469 (2018).
17. Dudas, J. *et al.* Quantum reservoir computing implementation on coherently coupled quantum oscillators. *npj Quantum Inf.* **9**, 64, DOI: [10.1038/s41534-023-00734-4](https://doi.org/10.1038/s41534-023-00734-4) (2023).
18. Govia, L., Ribeill, G., Rowlands, G., Krovi, H. & Ohki, T. Quantum reservoir computing with a single nonlinear oscillator. *Phys. Rev. Res.* **3**, 013077, DOI: [10.1103/PhysRevResearch.3.013077](https://doi.org/10.1103/PhysRevResearch.3.013077) (2021).
19. Dion, G., Mejaouri, S. & Sylvestre, J. Reservoir computing with a single delay-coupled non-linear mechanical oscillator. *J. Appl. Phys.* **124**, DOI: [10.1063/1.5038038](https://doi.org/10.1063/1.5038038) (2018).
20. Coulombe, J. C., York, M. C. & Sylvestre, J. Computing with networks of nonlinear mechanical oscillators. *PLoS one* **12**, e0178663, DOI: [10.1371/journal.pone.0178663](https://doi.org/10.1371/journal.pone.0178663) (2017).
21. Guo, X., Yang, W., Xiong, X., Wang, Z. & Zou, X. Mems reservoir computing system with stiffness modulation for multi-scene data processing at the edge. *Microsystems & Nanoeng.* **10**, 84, DOI: [10.1038/s41378-024-00701-9](https://doi.org/10.1038/s41378-024-00701-9) (2024).
22. Sun, J. *et al.* Novel nondelay-based reservoir computing with a single micromechanical nonlinear resonator for high-efficiency information processing. *Microsystems & Nanoeng.* **7**, 83, DOI: [10.1038/s41378-021-00313-7](https://doi.org/10.1038/s41378-021-00313-7) (2021).
23. Shima, K. *et al.* Improved learning performance in physical reservoir computing using coupled triple mems nonlinear resonators. In *2025 IEEE 38th International Conference on Micro Electro Mechanical Systems (MEMS)*, 546–549 (IEEE, 2025).
24. Bachtold, A., Moser, J. & Dykman, M. Mesoscopic physics of nanomechanical systems. *Rev. Mod. Phys.* **94**, 045005, DOI: [10.1103/RevModPhys.94.045005](https://doi.org/10.1103/RevModPhys.94.045005) (2022).
25. Cattiaux, D., Kumar, S., Zhou, X., Fefferman, A. & Collin, E. Geometrical nonlinearity of circular plates and membranes: An alternative method. *J. Appl. Phys.* **128**, DOI: [10.1063/5.0012329](https://doi.org/10.1063/5.0012329) (2020).
26. Maillet, O. *et al.* Measuring frequency fluctuations in nonlinear nanomechanical resonators. *ACS nano* **12**, 5753–5760 (2018).

27. Fedder, G. K., Hierold, C., Korvink, J. G. & Tabata, O. *Resonant MEMS: fundamentals, implementation, and application* (John Wiley & Sons, 2015).
28. Nikfarjam, H., Megdadi, M., Okour, M., Pourkamali, S. & Alsaleem, F. Energy efficient integrated mems neural network for simultaneous sensing and computing. *commun. eng.* **2**, 19 (2023).
29. Bai, Y., Yang, W., Zhu, B., Wang, Z. & Zou, X. A mems accelerometer with in-sensor neuromorphic computing capability. In *2025 23rd International Conference on Solid-State Sensors, Actuators and Microsystems (Transducers)*, 1720–1723 (IEEE, 2025).
30. Zheng, T. *et al.* Enhancing performance of reservoir computing system based on coupled mems resonators. *Sensors* **21**, 2961 (2021).
31. Mahboob, I., Nishiguchi, K., Okamoto, H. & Yamaguchi, H. Phonon-cavity electromechanics. *Nat. Phys.* **8**, 387–392 (2012).
32. Sun, F., Dong, X., Zou, J., Dykman, M. I. & Chan, H. B. Correlated anomalous phase diffusion of coupled phononic modes in a sideband-driven resonator. *Nat. communications* **7**, 1–8 (2016).
33. Zhou, X. *et al.* High-q silicon nitride drum resonators strongly coupled to gates. *Nano Lett.* **21**, 5738–5744 (2021).
34. Pokharel, A., Xu, H., Venkatachalam, S., Collin, E. & Zhou, X. Coupling capacitively distinct mechanical resonators for room-temperature phonon-cavity electromechanics. *Nano Lett.* **22**, 7351–7357 (2022).
35. Kumar, S., Cattiaux, D., Collin, E., Fefferman, A. & Zhou, X. Microwave optomechanically induced transparency and absorption between 250 and 450 mk. *J. Low Temp. Phys.* **210**, 562–572 (2023).
36. Appeltant, L. *et al.* Information processing using a single dynamical node as complex system. *Nat. communications* **2**, 468, DOI: [10.1038/ncomms1476](https://doi.org/10.1038/ncomms1476) (2011).
37. Xu, H. *et al.* Imaging nanomechanical vibrations and manipulating parametric mode coupling via scanning microwave microscopy. *Nano Lett.* **24**, 8550–8557 (2024).
38. Zhou, X., Cattiaux, D., Theron, D. & Collin, E. Electric circuit model of microwave optomechanics. *J. Appl. Phys.* **129**, DOI: [10.1063/5.0039624](https://doi.org/10.1063/5.0039624) (2021).
39. Barazani, B., Dion, G., Morissette, J.-F., Beaudoin, L. & Sylvestre, J. Microfabricated neuroaccelerometer: integrating sensing and reservoir computing in mems. *J. Microelectromechanical Syst.* **29**, 338–347 (2020).
40. Wringe, C., Trefzer, M. & Stepney, S. Reservoir computing benchmarks: a tutorial review and critique. *Int. J. Unconv. Comput.* **40**, 313–351 (2025).
41. Zheng, T. *et al.* Parameters optimization method for the time-delayed reservoir computing with a nonlinear duffing mechanical oscillator. *Sci. Reports* **11**, 997, DOI: [10.1038/s41598-020-80339-5](https://doi.org/10.1038/s41598-020-80339-5) (2021).
42. Venkatachalam, S. & Zhou, X. Effects of stochastic forces on the nonlinear behaviour of a silicon nitride membrane nanoelectromechanical resonator. *Nanotechnology* **34**, 215202, DOI: [10.1088/1361-6528/acbeb0](https://doi.org/10.1088/1361-6528/acbeb0) (2023).
43. Xu, H. *et al.* Fabrication of silicon nitride membrane nanoelectromechanical resonator. *Microelectron. Eng.* **280**, 112064, DOI: [10.1016/j.mee.2023.112064](https://doi.org/10.1016/j.mee.2023.112064) (2023).
44. Cucchi, M., Abreu, S., Ciccone, G., Brunner, D. & Kleemann, H. Hands-on reservoir computing: a tutorial for practical implementation. *Neuromorphic Comput. Eng.* **2**, 032002, DOI: [10.1088/2634-4386/ac7db7](https://doi.org/10.1088/2634-4386/ac7db7) (2022).

Acknowledgements (not compulsory)

The authors would like to acknowledge financial support from the French National Research Agency, ANR-MORETOME, No. ANR-22-CE24-0020-01, and Chist-ERA NOEMIA project with contract ANR-22-CHR4-0006-01. This work was partly supported by the French Renatech network. X.Z. also would like to thank Toky-Harrison Rabenimanana for his contributions in developing the reservoir computing setup.

Author contributions statement

X.Z. conceived the experiments and supervised the project. L.F. and X.Z. fabricated the samples in the clean room. P.L. and X.Z. developed the experimental setup. T.F., L.F., and X.Z. conducted the experiments and analyzed the results. All authors reviewed the manuscript and contributed to the discussions.

Additional information

5 Supplementary Information

5.1 Reservoir Computing based on the amplitude modulation of the force in the Duffing regime

Micro/nano-mechanical resonators have intrinsic nonlinear properties, coming from material properties and geometries. One well-known phenomenon is the Duffing behavior, in which the frequency response of MEMS under strong driving no longer follows the simple Lorentzian form. The motion equation of the resonator becomes :

$$\ddot{x} + \gamma_m \dot{x} + \Omega_m^2 x + \beta x^3 = \frac{F_d}{m_{eff}} \cos(\omega_d t) \quad (9)$$

where γ_m is the damping coefficient, Ω_m is the resonance frequency of the resonator, β is the Duffing nonlinearity coefficient normalized by the effective mass m_{eff} and F_d is the amplitude of the electrostatic force. For a circular membrane drum mechanical resonator (e.g. SiN drum or Al drum), the Duffing nonlinearity is primarily geometric in origin²⁵. In this work, we excite only the fundamental mode of the SiN drum in the Duffing nonlinear regime. No Duffing nonlinearity was observed in the Al drum resonator.

Figure 6 (a) shows the characteristic Duffing nonlinear frequency response of the SiN drum resonator when driven by a relatively large electrostatic force. For $\beta > 0$, strong driving causes the resonance frequency to shift toward higher values, and the frequency response exhibits hysteretic behavior between forward (black curve) and backward (red curve) frequency sweeps. The hysteresis window is bounded by two saddle-node bifurcation points, within which stochastic switching between bistable states can arrive⁴². For reservoir computing experiments, the operating frequency is chosen outside the bistable region at $\Omega_d/(2\pi) = 12.257$ MHz, as indicated by the dashed line in Fig. 6 (a). By fixing the drive frequency at this value, we measure the mechanical response as a function of the driving force amplitude V_d , as shown in Fig. 6 (b). Based on this response, three different driving-force modulation windows are selected for evaluating the reservoir computing performance. The *M3* represents the whole window with variations of the drive amplitude between 0 and 16 mV where the curve shows a clear nonlinear profile. Similarly, the *M1* showcases nonlinear variations, it is proper to drive voltage amplitudes less than 9 mV thus limiting the electrostatic drive force to smaller values. Lastly, in the *M2* the variation of the mechanical response of the SiN membrane as a function of the drive amplitude is almost linear.

When the *M3* modulation window is used, near-perfect success rates are achieved from the first-order (P_1) to the fourth-order (P_4) parity benchmarks, owing to the strong nonlinear variations present in this regime. As for the window *M1*, the results surpass a value of 90 % for P_1 and P_2 indicating successful predictions by our system. However, they drop to approximately 58 % starting from P_3 . Moreover, for *M2* where there is an absence of nonlinearity, the results are less important reaching 70 % for P_2 and then dropping quickly to approximately 59 % starting from P_3 . The same conclusion can be taken, the optimal results are obtained in the modulation window that exhibits the most amount of nonlinearity in the amplitude-amplitude curve.

5.2 Two-tone driving scheme

The coupled electromechanical resonators act as capacitor $C_g(X_1, X_2)$ consisting of 2 moving membranes. The mechanical displacement amplitudes are expressed as $X_1(t)$ and $X_2(t)$ respectively for each of the SiN and Al drum resonators resonating at frequencies Ω_1 and Ω_2 . The motion equation of this double-drum resonator is described by

$$\begin{aligned} \ddot{X}_1 + \gamma_1 \dot{X}_1 + \Omega_1^2 X_1 &= \frac{V_{ac} V_{dc}}{m_1 d} C_{go} \left[1 - 2 \frac{(X_2 - X_1)}{d} \right], \\ \ddot{X}_2 + \gamma_2 \dot{X}_2 + \Omega_2^2 X_2 &= \frac{V_{ac} V_{dc}}{m_2 d} C_{go} \left[-1 + 2 \frac{(X_2 - X_1)}{d} \right]. \end{aligned} \quad (10)$$

In the blue sideband pumping scheme, $\Omega_p = \Omega_1 + \Omega_2 + \Delta$, we probe the Al drum at the frequency $\Omega_d = \Omega_2 + \delta$. The mechanical displacement x_1 and x_2 corresponding respectively to the unprobed and probed resonators are established as follows:

$$\begin{aligned} x_1 &= -\frac{f_p}{2m_1 \Omega_1} \frac{x_2^*}{d} \chi_1, \\ x_2 &= -\frac{f_d}{2m_2 \Omega_2} \frac{1}{\chi_2 - \frac{|f_p|^2 \chi_1^*}{4m_1 m_2 d^2 \Omega_1 \Omega_2}}. \end{aligned} \quad (11)$$

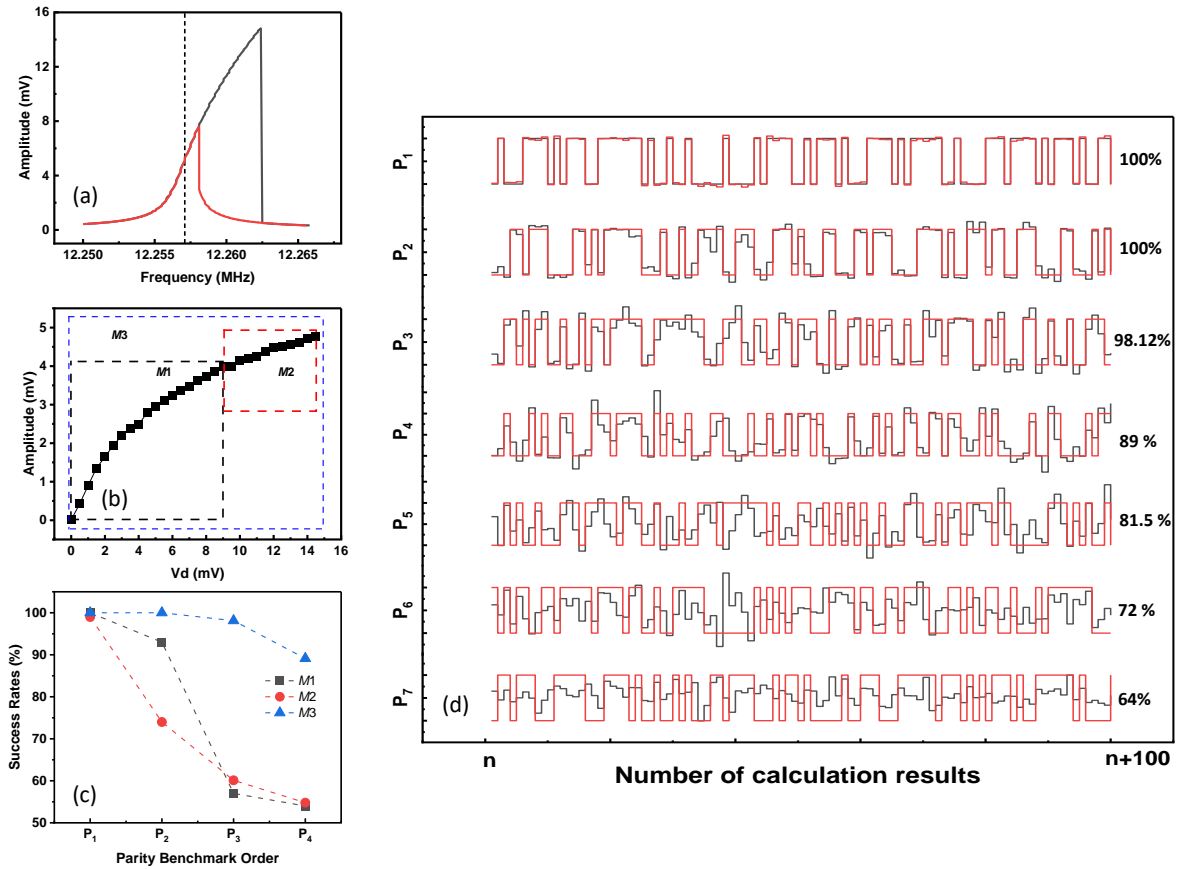


Figure 6. Reservoir Computing based on Duffing nonlinearity. (a) The mechanical response of the SiN resonator as a function of the frequency for $V_d = 15$ mV, attenuated by 20 dB. The red curve corresponds to the reverse frequency sweep and the black curve corresponds to the forward sweep. (b) The variation of the mechanical response of the resonator as a function of the drive voltage at the frequency $\Omega_d/(2\pi) = 12.257$ MHz. The curve is divided into 3 modulation windows of the electrostatic force applied: $M1$, $M2$ and $M3$. (c) The results of reservoir computing based on the modulation of the electrostatic drive force in the Duffing nonlinear regime for the 3 different modulation windows. (d) Comparison between the target output in red and the predicted output after training the output weights in black, which are obtained in the modulation window $M3$.

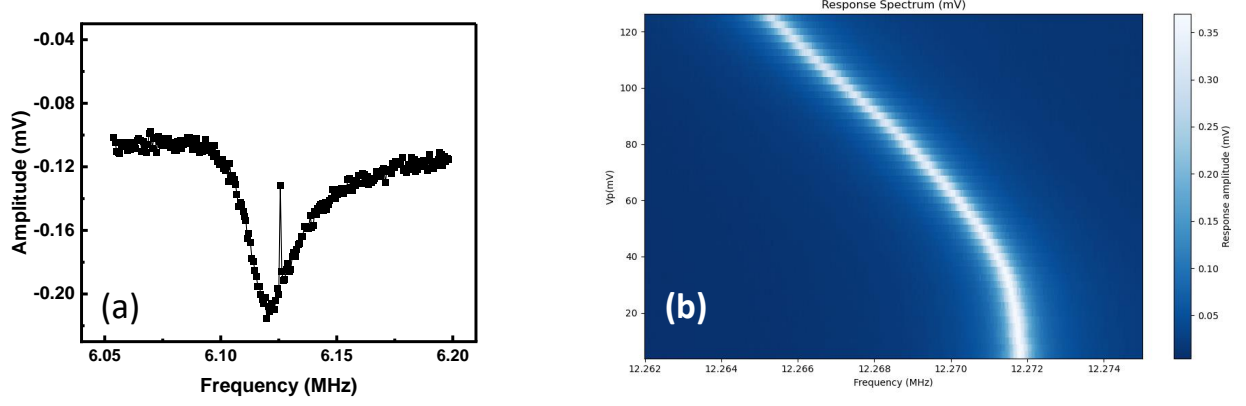


Figure 7. (a) Frequency responses of Al drum measured $V_d = 80$ mV, when the phonon-cavity is pumped at its blue sideband at frequency $\Omega_p = \Omega_1 + \Omega_2 = 2\pi \times 18.3$ MHz and a pump amplitude of $V_p = 0.11$ V. (b) The 2D plots of the frequency responses of the SiN drum resonator corresponding to different blue sideband pump amplitudes.

The $f_p = \frac{C_{g0}V_{dc}\mu_p}{d}$ and $f_d = \frac{C_{g0}V_{dc}\mu_d}{d}$ are the complex amplitudes of the pumping and the driving forces. The definition of the mechanical susceptibilities become:

$$\begin{aligned} \chi_1 &= \frac{1}{\delta - \Delta - i\frac{\gamma_1}{2}}, \\ \chi_2 &= \frac{1}{-\delta - i\frac{\gamma_2}{2}}. \end{aligned} \tag{12}$$

All derivation details have been reported in our previous work³⁴.

In the two-tone scheme, the interference window is primarily determined by the bandwidths of the two coupled modes, as reflected in the denominators of Eqs. 11 and 12. For the case of probing Al drum, the bandwidth of SiN γ_{SiN} is much smaller than that of Al drum, $\gamma_{SiN} \ll \gamma_{Al}$. As a result, the interference effect induced by blue-sideband pumping appears as a narrow peak within the broader bandwidth of the Al drum³⁴. The pump frequency is set to $\Omega_{SiN} + \Omega_{Al} + \delta$. When the swept probe frequency around the Al drum resonance reaches $\Omega_{Al} + \delta$, this interference effect becomes clearly observable, as shown in Fig.7(a).

In the sideband pumping scheme, the resonance frequency of the coupled drum resonator will shift because the pump amplitude modifies the susceptibility of the electromechanical resonator³⁴. It is well-known in the optomechanical system, so called the optical spring effects. In the blue sideband pump scheme, we sweep frequency responses of the SiN drum corresponding to different pump amplitudes. As present in the Fig 7(b), the maximal resonance frequency Ω_{SiN} decreases from $2\pi \times 12.272$ MHz to $2\pi \times 12.265$ MHz when the pump amplitude increases from 0 V to 125 mV. This $2\pi \times 7$ kHz shift is still within the bandwidth of the Al membrane ($\gamma_2 \approx 2\pi \times 25.9$ kHz), however, it is much larger than that of the SiN membrane ($\gamma_1 \approx 2\pi \times 944$ Hz). In the two-tone scheme, the modulations of the pump amplitudes therefore can bring the probe tone into or out of the interference window, thereby forming a controllable nonlinear response.